Federation
UNIVERSITY•AUSTRALIA

COPYRIGHT NOTICE

FedUni ResearchOnline
https://researchonline.federation.edu.au

This is the published version of:

Zhao, Z., Yao, C., Tang, C., Li, C., Yan, F., Islam, S. (2019) Diagnosing transformer winding deformation faults based on the analysis of binary image obtained from FRA signature. IEEE Access, 7, p. 40463-40474.

Available on at https://doi.org/10.1109/ACCESS.2019.2907648

Diagnosing Transformer Winding Deformation Faults Based on the Analysis of Binary Image Obtained From FRA Signature

ZHONGYONG ZHAO[ID][1], **CHENGUO YAO**[ID][2], **(Member, IEEE), CHAO TANG**[1],
CHENGXIANG LI[2], **FAYOU YAN**[ID][1], **AND SYED ISLAM**[3], **(Fellow, IEEE)**

[1]College of Engineering and Technology, Southwest University, Chongqing 400716, China
[2]State Key Laboratory of Power Transmission Equipment and System Security and New Technology, Chongqing University, Chongqing 400044, China
[3]School of Science Engineering and Information Technology, Federation University Australia, Melbourne, VIC 3353, Australia

Corresponding author: Zhongyong Zhao (zhaozy1988@swu.edu.cn)

ABSTRACT Frequency response analysis (FRA) has been widely accepted as a diagnostic tool for power transformer winding deformation faults. Typically, both amplitude-frequency and phase-frequency signatures are obtained by an FRA analyzer. However, most existing FRA analyzers use only the information on amplitude–frequency signature, while phase–frequency information is neglected. It is also found that in some cases, the diagnostic results obtained by FRA amplitude–frequency signatures do not comply with some hard evidence. This paper introduces a winding deformation diagnostic method based on the analysis of binary images obtained from FRA signatures to improve FRA outcomes. The digital image processing technique is used to process the binary image and obtain a diagnostic indicator, to arrive at an outcome for interpreting winding faults with improved accuracy.

INDEX TERMS Frequency response analysis, power transformers, windings, binary image, fault identification.

I. INTRODUCTION

As the heart of a substation, a power transformer functions as the significant link for voltage conversion and energy delivery. Survey results show that most power transformers worldwide were installed in the 1980s, and many of them are reaching the end of their life [1]. The failure rate of these transformers has been persistently increasing in recent years, particularly in utilities with poor maintenance and asset management regimes. One of the key factors that induce transformer failure is winding deformation. The typical types of winding deformation are tilting, forced bulking, free buckling, forced buckling, hoop tension, and telescoping. These winding deformations are typically due to large electromagnetic forces induced by the short circuit currents [2]. Normally, the initial stage of winding deformation is characterized by winding minor deformation. Winding minor

The associate editor coordinating the review of this manuscript and approving it for publication was Boxue Du.

deformation will have limited impact on the normal operation of a power transformer, and it is difficult to detect and diagnose these faults. However, the minor deformation can develop into catastrophic failure if no steps are taken. Thus, it is of significance to detect winding deformation faults when they are at the early stage.

Several winding deformation fault detection methods have been successively proposed in recent years. To date, major detection methods consist of vibration method [3], ultra-wideband (UWB) antenna method [4], short circuit impedance (SCI) method [5], [6], low voltage impulse (LVI) method [7] and frequency response analysis (FRA) method [8]. Of all these methods, FRA is now widely accepted as the most superior method for winding movement related fault detection in transformers. According to the nature of the FRA input signal, FRA can be divided into sweep FRA (SFRA) and impulse FRA (IFRA) [9]. In both FRA methods, the frequency response signatures of the transformer are obtained by injecting the excitation signal to the

winding and measuring the response signal. The difference is that the SFRA uses a sinusoidal sweep signal for excitation, while IFRA uses an impulse signal for excitation.

Among the above methods, FRA is a reliable, simple, fast, economic and non-destructive diagnostic tool [10]. IFRA has reached potential for online application; however, it is currently at the rapid developmental phase [9], [11]. SFRA is discussed the most in the literature, and is frequently referred to FRA. FRA has been under development for years. Chinese power industry standard [12] and IEC standard [13] have been successively proposed to standardize the technique. This method is widely accepted by power equipment owners, operators, producers and testing companies. However, there still exist some problems when FRA is applied in the field.

- The FRA signatures of a power transformer measured by an FRA analyzer normally include the amplitude–frequency and phase–frequency characteristic signature. Only the variation of amplitude–frequency signature is analyzed in the existing diagnostic method, and the information of phase–frequency signature is mostly neglected [14].
- The FRA interpretation relies on graphical comparison, namely, analyzing the variation between the FRA signatures and the reference. The current comparison process calls for experienced personnel, as there is no standard and automatic interpretation code to date. When the FRA amplitude–frequency signature is used for diagnosing a winding minor deformation fault, the variation of signature is not remarkable, and as a result, it is hard to detect using visual inspection, which makes the diagnostic result obtained by conventional FRA technique inaccurate. Although the detection sensitivity can be improved by extending FRA frequency ranges [15], the FRA frequency band beyond 1 MHz is easily affected by the external factors, for instance the FRA equipment wiring, parasitic impedance, noise, *etc* [16]. Thus, improving FRA sensitivity by extending the upper limit of frequency is not an optimum method.

To solve above problems, researchers have recently introduced some novel and improved methods. M. H. Samimi *et al.* have proposed improved numerical indices for the FRA interpretation by including phase response, in which a new diagnostic index, complex distance, was introduced in addition to a method to include the phase information [17]. It was demonstrated that using the phase data increases the sensitivity of the indices versus mechanical displacements. O. Aljohani *et al.* have introduced a novel FRA interpretation approach to detect transformer winding short-circuit fault, radial deformation and bushing faults by using polar plot and digital image processing, in which the various image unique features of a polar plot are extracted using geometric dimensions, invariant moments and texture analysis to construct diagnostic metrics [18]–[20]. It was found that the polar plot exhibits more features than the magnitude of the FRA signature, and the investigated

metrics are consistently increasing with the increase in fault level. The above outcomes are significant contributions for improving the performance of FRA diagnostics. However, in complex distance index, the FRA phase information is included in a specific equation, not intuitively presented in a waveform or image. Nevertheless, the practical validation of a small dry–type transformer is performed in the latter finding, but most FRA data of winding faults are acquired by a 3-D finite-element analysis (FEA) of transformers, and are not verified in a large oil-immersed power transformer.

In view of the above background, this study investigates a winding deformation diagnostic method based on the analysis of binary image obtained from the FRA signature. The FRA amplitude–frequency and phase–frequency signatures are used to construct plane polar plots. The digital image processing technique is used to process polar plots to outcome binary images, which can be analyzed to diagnose and identify the winding deformation faults. In this study, all FRA raw data are obtained from actual transformer measurements, including a specially manufactured transformer that can emulate variable winding faults and two large oil-immersed power transformers.

II. THEORETICAL ANALYSIS
A. BASIC PRINCIPLE
The FRA signature is obtained by a sweep frequency approach. The sinusoidal sweep frequency excitation voltage with an amplitude of <20 V is applied to one terminal of transformer winding and the response voltage at the other terminal is measured. The excitation signal and response signal under the same frequency point are used to plot an amplitude–frequency and a phase–frequency characteristic signature, as shown in Equation (1)-(2) [10], [16],

$$H_\mathrm{f} = 20 \log_{10} \frac{|U_2(f)|}{|U_1(f)|} \tag{1}$$

$$\varphi_\mathrm{f} = \varphi(U_2(f)) - \varphi(U_1(f)) \tag{2}$$

where $U_1(f)$ and $U_2(f)$ are the excitation voltage and response voltage of tested winding; H_f is the amplitude–frequency characteristic signature; $\varphi()$ is the angle of signal; φ_f is the phase–frequency characteristic signature; and f represents different frequency.

Plane polar plot consists of polar radius coordinate and polar angle coordinate, represented by (ρ, θ). The method of constructing polar a plot of frequency response is that the polar radius and polar angle are equivalent to the amplitude and phase of frequency response, respectively. Thus, the vertical projection of the polar plot along X axis and Y axis under frequency f can be defined as Equation (3)-(4),

$$x_\mathrm{f} = |H_\mathrm{f}| \cdot \cos(\varphi_\mathrm{f}) \tag{3}$$

$$y_\mathrm{f} = |H_\mathrm{f}| \cdot \sin(\varphi_\mathrm{f}) \tag{4}$$

where x_f is the vertical projection of the polar plot along X axis under specific frequency f; y_f is the vertical projection of the polar plot along Y axis under specific frequency f.
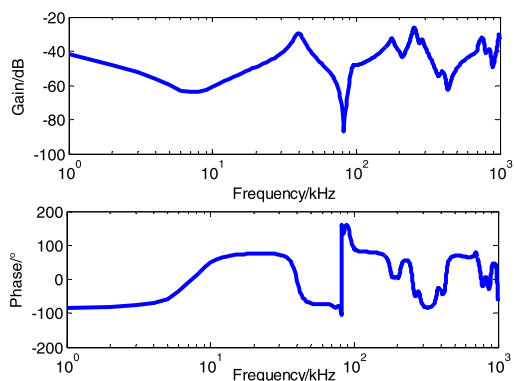
FIGURE 1. FRA amplitude-frequency characteristic and phase-frequency characteristic signature of a transformer winding.

It can be demonstrated that Equation (3) and (4) are fit for various values of φ_f, namely, φ_f lies in four different quadrants.

As the information of amplitude and phase of frequency response are included in the plane polar plot [18], the sensitivity of using polar plot to diagnose winding fault may be higher than the current traditional FRA method, which only considers the amplitude–frequency characteristic signature [17]–[18].

The typical amplitude–frequency characteristic and phase–frequency characteristic signature of a power transformer is shown in Fig. 1. There exist multiple resonances and anti-resonances between 1 and 1000 kHz. According to Chinese power industry standard [12], the frequency band of FRA could be divided into low frequency band (1 $\sim$ 100 kHz), middle frequency band (100 $\sim$ 600 kHz) and high frequency band (600 $\sim$ 1000 kHz) for interpretation. The FRA low frequency band is characterized by the transformer inductive components because flux penetration to the core is significant within this frequency range, the FRA high frequency band is dominated by the transformer distributed capacitive components, while the FRA middle frequency band is characterized by inductive, as well as capacitive, components [9], [12], [16]. According to above standard, the polar plot that corresponds to this FRA signature is presented in Fig. 2. The upper two sub-figures are the polar plot of an entire frequency band and the polar plot of 1 to 100 kHz, and the lower two sub-figures are the polar plot of 100 to 600 kHz and the polar plot of high frequency band 600 to 1000 kHz.

B. DIAGNOSTIC PROCEDURE OF WINDING DEFORMATION FAULT

The proposed procedure of diagnosing transformer winding deformation fault is shown in Fig. 3. The procedure also relies on graphical comparison of winding healthy and faulty transformer binary images.

Step 1: The FRA data of power transformer under healthy and faulty status are accurately measured by an FRA analyzer, including amplitude–frequency and phase–frequency signatures. The frequency range is selected as 1 $\sim$ 1000 kHz, and
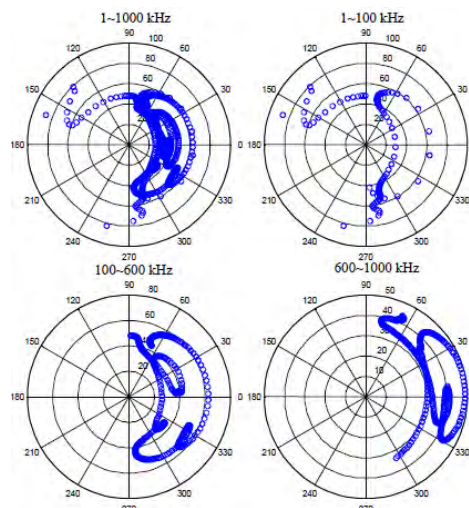

FIGURE 2. Polar plot of variable frequency bands which corresponds to transformer frequency response signature.
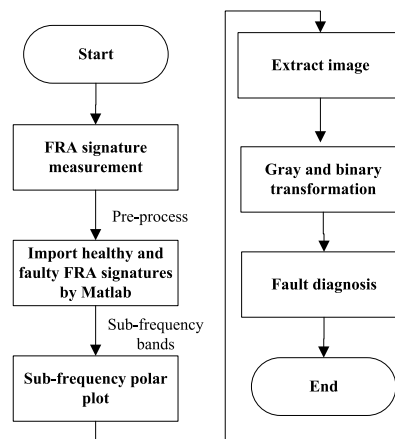

FIGURE 3. Flow chart for diagnosis of proposed method.

frequency interval is no less than 2 kHz [12]. A linear fitting moving average method can be adopted to preprocess the FRA raw data, and the large burrs are smoothed to decrease the effect of external disturbance [21].

Step 2: The frequency response data of healthy and faulty transformer are imported to MATLAB software.

Step 3: The polar plots that correspond to 1 $\sim$ 100 kHz, 100 $\sim$ 600 kHz and 600 $\sim$ 1000 kHz frequency ranges are plotted, respectively.

Step 4: Image extraction. The polar plots can be transferred into plane Cartesian coordinate system. The background of the MATLAB figure is set as white color, and the coordinate axes are removed. The three primary colors (red, green, blue, RGB) pattern diagram of frequency response polar plot is then obtained. Considering that there may be significant differences between images of healthy and faulty winding under the individual sub-frequency range, it is meaningful to compare two images under the same image scale. The image scale factor k is defined. The extents of RGB image under the

sub-frequency range can be obtained by

$$\begin{cases} x'_{max} = x_{max} + |x_{max} - x_{min}| / k \\ x'_{min} = x_{min} - |x_{max} - x_{min}| / k \\ y'_{max} = y_{max} + |y_{max} - y_{min}| / k \\ y'_{min} = y_{min} - |y_{max} - y_{min}| / k \end{cases} \quad (5)$$

where x'_{max} and x'_{min} are the maximum and minimum value of the Cartesian coordinate horizontal axis corresponding to the image border after the RGB image is scaled, respectively; y'_{max} and y'_{min} are the maximum and minimum value of the Cartesian coordinate vertical axis corresponding to the image border after the RGB image is scaled, respectively; x_{max} and x_{min} are the maximum and minimum value of the Cartesian coordinate horizontal axis corresponding to the image border before the RGB image is scaled, respectively; y_{max} and y_{min} are the maximum and minimum value of the Cartesian coordinate vertical axis corresponding to the image border before the RGB image is scaled, respectively. The test demonstrates that the performance is good when image scale factor k is between 8 and 15, and the value of k is selected as 10 in this study.

Step 5: Image gray and binary transformation is performed. The RGB image obtained by step 4 is first processed by gray transformation, and the gray image of frequency response is obtained. The gray image is then transformed into a binary image. The data matrix which corresponds to the binary image consists of "1" and "0", "1" represents background pixels of the image, while "0" represents the corresponding pixels of the frequency response. Fig. 4 shows the binary image obtained from polar plot of Fig. 2, the frequency band is $100 \sim 600$ kHz, the dash line of Fig. 4 is the border of the scaled image.

Step 6: Fault diagnosis. Fault diagnosis is realized by comparison of the binary image with its referenced image. To quantify and standardize the diagnosis process, the binary images of different frequency ranges are further analyzed by introducing a correlation indicator (*ci*). Specifically, the matrix similarity is used to process the data matrix of binary images, and the formula is given as,

$$ci = \frac{\sum_m \sum_n (A_{mn} - \bar{A})(B_{mn} - \bar{B})}{\sqrt{\left(\sum_m \sum_n (A_{mn} - \bar{A})^2\right)\left(\sum_m \sum_n (B_{mn} - \bar{B})^2\right)}} \quad (6)$$

where *ci* represents the matrix similarity; *m* and *n* are the row and column of the matrix; A_{mn} and B_{mn} are the elements of the matrix A and B, respectively; $\bar{A}$ and $\bar{B}$ are the average values of all elements of matrix A and B, respectively.

The distribution of *ci* of healthy and faulty binary images under individual frequency ranges can then be analyzed to diagnose winding deformation fault.

In the current conventional FRA technique, variable statistical indicators are proposed to interpret FRA signatures, for instance, the correlation coefficient, standard deviation, variance, standard error of mean, root mean square, *et.al* [22].
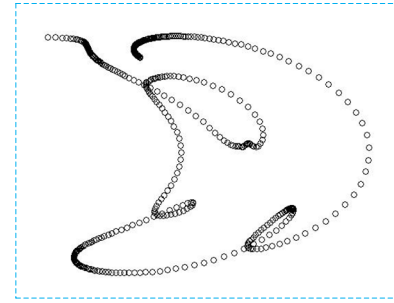

FIGURE 4. Binary image obtained from polar plot of Fig. 2 in middle frequency band.
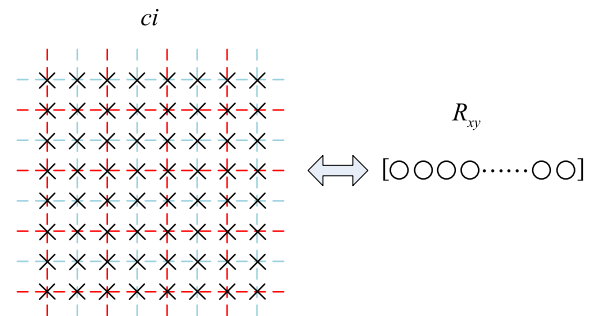

FIGURE 5. Difference between the distributions of data corresponding to *ci* and R_{xy} indicators.

Of all these indices, the Chinese standard DL/T 911 suggests relative factor (R_{xy}) as the diagnostic indicator [12].

For the two FRA amplitude–frequency traces X_i and Y_i, the R_{xy} is defined as follows [23],

$$R_{xy} = \begin{cases} 10 & 1 - P_{xy} < 10^{-10} \\ -\log_{10}(1 - P_{xy}) & \text{otherwise} \end{cases} \quad (7)$$

where P_{xy} is given by,

$$P_{xy} = \frac{\frac{1}{N}\sum_{i=1}^{N}(X_i - \frac{1}{N}\sum_{i=1}^{N}X_i) \cdot (Y_i - \frac{1}{N}\sum_{i=1}^{N}Y_i)}{\sqrt{D_x D_y}} \quad (8)$$

and D_x and D_y are defined as,

$$D_x = \frac{1}{N}\sum_{i=1}^{N}(X_i - \frac{1}{N}\sum_{i=1}^{N}X_i)^2 \quad (9)$$

$$D_y = \frac{1}{N}\sum_{i=1}^{N}(Y_i - \frac{1}{N}\sum_{i=1}^{N}Y_i)^2 \quad (10)$$

ci is an indicator that computes the 2-D "0-1" data matrix of binary image, while R_{xy} is an indicator that computes the 1-D vector data of FRA amplitude–frequency signature. The difference between the distributions of data corresponding to two indicators is visually presented in Fig. 5. In Fig. 5, "x" is the data of binary image with values of 0 and 1, which represent the frequency response and background, respectively. "O" represents the amplitude data of the

TABLE 1. Design specifications of specifically manufactured model transformer.

Parameters		Nominal value
Rated voltage(kV)		10/0.4
Capacity(kVA)		400
Rated current(A)		23/577
Frequency(Hz)		50
Number of phase		3
Connection type		Ynyn0
Tank(mm)		1705×740×1415
HV winding	Outer radius(mm)	250
	Inner radius(mm)	210.5
	Height(mm)	519
LV winding	Outer radius(mm)	174.5
	Inner radius(mm)	158
	Height(mm)	363
Iron core	Yoke radius(mm)	150
	Yoke height(mm)	1190
	Yoke length(mm)	1390

FIGURE 6. Tested model transformer with its tank uncovered.

FIGURE 7. Images of actual RD winding. (a) 10% RD fault degree with fault happened in one direction. (b) 5% RD fault degree with fault happened in 3 directions.
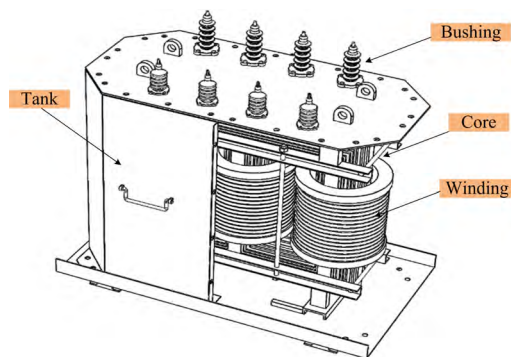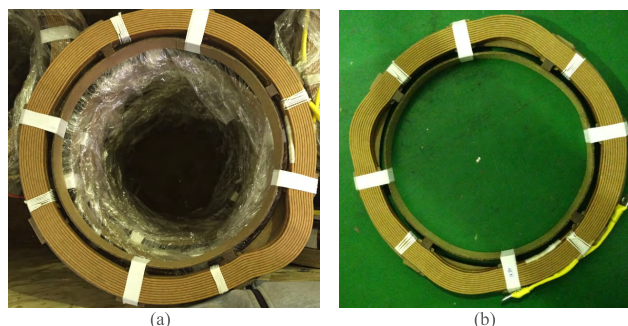
FRA signature. Obviously, 2-D ''0-1'' data matrix comprises the amplitude as well as phase information of frequency response.

In addition, it can be concluded from Fig. 5 and Eq. (6) that the proposed binary image method analyzes the FRA data and background from a mathematical point of view. The calculation of proposed binary image method is easy and fast, which may be suitable for field application.

III. TEST PLATFORM OF EMULATING POWER TRANSFORMER WINDING DEFORMATION FAULT AND FRA SIGNATURES OF TYPICAL WINDING FAULTS

It is possible to precisely analyze the behavior of transformer windings by emulating the winding faults in actual transformers. A test platform was built to perform groups of winding deformation fault experiments in [21] and [24]. The tested transformer is a specially manufactured core-type model transformer with a voltage ratio of 10/0.4 kV. Some nameplate parameters can be found in Tab. 1. The internal configuration of the model transformer is designed as that of a 110 kV power transformer, as shown in Fig. 6. The HV winding is a disk type winding with a total of 30 disks, where the upper and lower 10 disks are interleaved twist and the middle 10 disks are sequential twist. The LV winding is designed as a layer type with 6 layers. Variable windings were also manufactured, which can be used to replace the middle 10 disks winding to emulate diverse winding radial deformation faults.

Typical winding radial deformation (RD) fault, inter-disk short circuit (SC) fault and disk space variation (DSV) fault were simulated, respectively.

In winding RD fault, the middle twisted windings are replaced by other manufactured deformed windings, including different fault degrees and fault directions. Fig. 7 shows some images of actual RD winding, where the size and position of radial deformed part is variable to emulate different fault degree and direction. More detailed information about winding RD fault setup can be found in [21]. Winding inter-disk SC fault is simulated by simply shortening the connectors of the middle sequential twist windings; the greater the number of connectors that are shortened, the closer the severity of inter-disk SC fault. Shortening winding disks for emulating the inter-disk SC fault changes the turns of winding and the distribution of leakage magnetic field. Thus, the self-inductance and mutual-inductance are changed, which contributes to the variation of winding FRA signature.

Reference [25] indicates that winding DSV fault is normally characterized by the reduction of disk space distance, the inter-disk capacitance and mutual inductance of winding equivalent electrical model increase. Thus, for simulating this type of fault, a capacitor is connected to the connectors of two continuous disks. The connected capacitor mainly increases the inter-disk capacitance. There also exists a new path for the current that flows through the winding, and the distribution of leakage magnetic field is changed. Thus, indirectly, the mutual inductance parameter of the winding equivalent electrical model is changed. The inter-disk capacitance of healthy sequential twist windings is calculated as approximately 2 nF based on the finite element method (FEM),
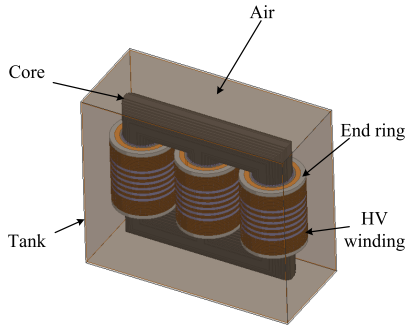
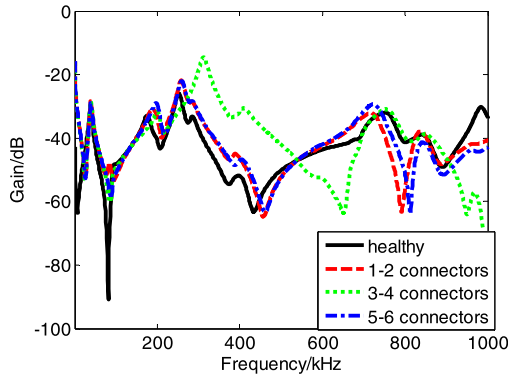**FIGURE 8.** FEM model for calculating inter-disk capacitance of healthy windings.

FIGURE 9. Some cases of FRA amplitude-frequency signatures under simulated winding inter-disk SC fault.
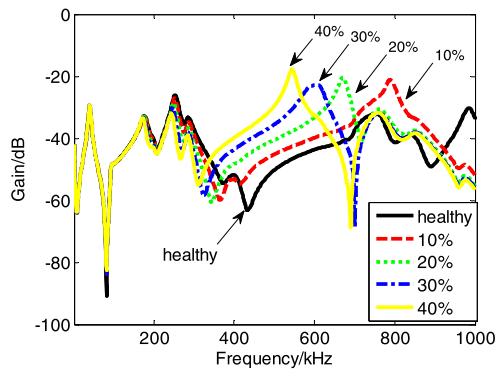

FIGURE 10. Some cases of FRA amplitude-frequency signatures under simulated winding DSV fault.

the FEM model is shown in Fig. 8. Otherwise, the degree of DSV fault is emulated by increasing and decreasing the capacitance value, and the fault location is emulated by changing the sequence numbers of the two connectors.

End-to-end open circuit measurements were performed in the HV winding of phase A with various fault statuses of the model transformer, and a sample database was obtained. Various FRA signatures of simulated winding deformation are shown in Figs. 9-11.

Fig. 9 shows some cases of FRA amplitude–frequency signatures under simulated inter-disk SC fault, in which "1-2 connectors" means that the first and second connectors
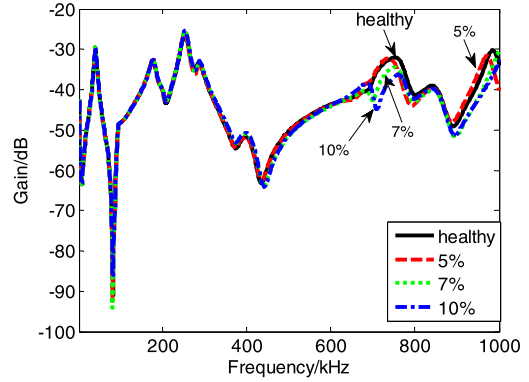

FIGURE 11. Some cases of FRA amplitude-frequency signatures under simulated winding RD fault.

of the middle sequential twist windings are short circuited, seen from top to bottom. Fig. 9 shows that FRA signatures of inter-disk SC fault are entirely different throughout the entire frequency band compared to a healthy signature. Moreover, the FRA signatures of the "1-2 connectors" and "5-6 connectors" are similar because these two fault cases are artificially manufactured in the symmetrical position of the HV winding.

Fig. 10 shows some cases of FRA amplitude–frequency signatures under simulated DSV faults. The fault simulated capacitor is paralleled with the third and fourth connectors of the middle sequential twist disks of HV phase A winding. 10% indicates the percentage of the paralleled capacitance (200 pF) to the capacitance of the adjacent healthy disk (2 nF), with similar meanings for 20% ∼ 40%. In Fig. 10, the faulty signature changes notably in the middle and high frequency bands, compared to the healthy FRA signature. The variations in the faulty signature become more noticeable as the fault level increases. Furthermore, the faulty FRA signature shifts toward the low frequency band. The changing trend of above FRA signatures is consistent with the trend described in [25], which also demonstrates the feasibility of emulating DSV fault.

Fig. 11 shows some cases of FRA amplitude–frequency signatures under simulated RD faults, in which the middle 10 disks healthy windings of HV phase A are replaced by RD fault windings with degrees of 5%, 7% and 10%, all in one direction. Fig. 11 illustrates that the faulty FRA signature changes in the middle and high frequency bands, and the difference is particularly remarkable beyond 700 kHz; both the frequency and gain of resonant points shift for a certain extent. The changing trend of above FRA signatures is consistent with the trend described in [12], [26], and [27], which also demonstrates the feasibility of emulating RD fault.

IV. ANALYSIS OF WINDING TYPICAL FAULT EXPERIMENTS

A. TYPICAL CASE

The polar binary images obtained from FRA signature of winding RD fault (5%) is shown in Fig. 12, this figure also presents the binary images corresponding to the FRA signature of a healthy winding. In Fig. 12(a) and (b), the binary
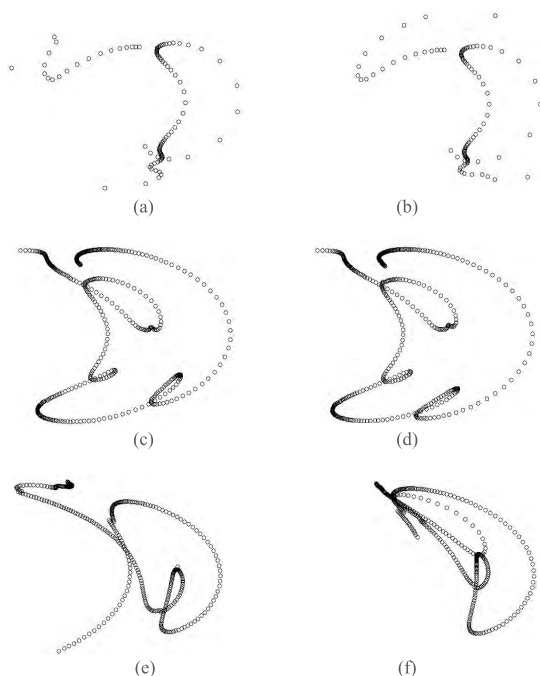
FIGURE 12. Frequency response binary image of healthy winding and 5% RD fault winding. (a) 0 ~ 100 kHz of healthy winding, (b) 0 ~ 100 kHz of deformed winding, (c) 100 ~ 600 kHz of healthy winding, (d) 100 ~ 600 kHz of deformed winding, (e) 600 ~ 1000 kHz of healthy winding, (f) 600 ~ 1000 kHz of deformed winding.

image is relatively sparse, and there exists few inflection points on the trace of image. The reason is that there is a small quantity (100 groups) of frequency response data points within the low frequency range, and the number of resonant points is limited. In contrast, in Fig. 12(c) ~ (f), the binary images are relatively intensive, and there exist more inflection points on the trace of the image. Correspondingly, more frequency response data points (600 and 500 groups) and numbers of resonant points within middle and high frequency bands contribute to this particular phenomenon. Additionally, in Fig. 12, binary images of healthy and faulty windings in low and middle frequency bands are very similar, while the difference between two binary images in high frequency band is significant.

The R_{xy} of healthy and faulty FRA amplitude–frequency signature, which corresponds to Fig. 12, has been evaluated within various frequency bands, which is shown in Tab. 2. Although the R_{xy} of high frequency band is much less than those of the middle and low frequency bands, according to the Chinese standard [12], the status of winding is still diagnosed as healthy. The diagnostic result is not consistent with the actual experimental setup of winding RD fault. This case indicates that there might be false positives and false negatives in the diagnostic result when traditional FRA method is used to detect winding faults.

The c_i of two binary images, which correspond to the healthy and faulty winding of Fig. 12, has also been evaluated within three frequency bands, as also presented in Tab. 2. Clearly, the c_i of two binary images in high frequency band is

TABLE 2. Relative factor of frequency response and correlation indicator of binary image corresponding to figure 12.

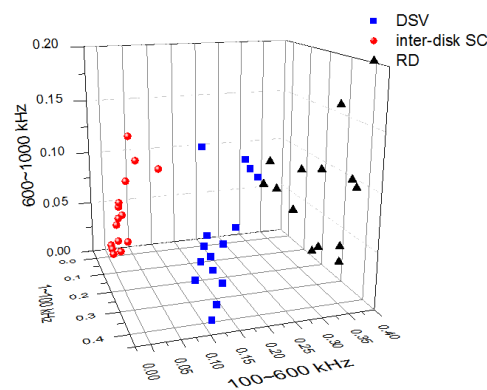| Method	Indicator	Frequency bands		
		1~100kHz	100~600kHz	600~1000kHz
FRA	R_{xy}	3.0547	2.0887	0.7721
Binary image	ci	0.3541	0.3146	0.0421

FIGURE 13. Distribution of correlation indicators of healthy and faulty frequency response binary images in all experimental setup.

considerably less than those of the middle and low frequency bands, which indicates there could exist some abnormalities in the tested winding. However, the threshold value that is required for evaluating the winding status needs to be concluded from extensive tests, yet it can still be derived that the variance of c_i in high frequency band to c_i of middle and low frequency band is closed to one order of magnitude. Apparently, the proposed method is more sensitive to the winding fault than the traditional FRA method.

B. ANALYSIS OF EXPERIMENTAL RESULT
For the simulated winding fault experiments performed in section III. A total of 42 groups of experiments were conducted. The groups of inter-disk SC faults is 15, including variable fault extent and fault locations setup. The combination of simulated RD status is extensive; however, to match the numbers of inter-disk SC fault, the groups of RD fault is set as 13, and the groups of DSV fault is 14, including variable fault extent and fault locations setup as well. In each fault experimental setup, the FRA amplitude–frequency as well as phase–frequency signatures are measured, the binary image is plotted based on the proposed procedure, and the c_i of healthy and faulty binary images under low, middle and high frequency band are obtained, respectively.

The c_i of sub-frequency binary images obtained from all the above experimental FRA signatures are plotted in Fig. 13, in which X axis varies from 1 to 100 kHz, Y axis varies from 100 to 600 kHz, and Z axis varies from 600 to 1000 kHz. It can be concluded that the distribution of c_i corresponding to each type of fault is not consistent in 3-dimensional spaces, which is due to a certain span in simulating winding fault.

TABLE 3. Effect of various faults on correlation indicator corresponding to figure 13.

Fault type	Frequency band(ci)		
	1~100kHz	100~600kHz	600~1000kHz
Inter-disk SC	<0.1	<0.1	<0.1
DSV	>0.2	<0.2	<0.2
RD	>0.2	>0.2	<0.2

In other words, there exists a certain interval between fault extents. In addition, the distribution of ci, which corresponds to each winding fault, is gathered. For instance, all ci of inter-disk SC fault in sub-frequency bands are relatively small. The ci of DSV fault is larger (>0.2) in low frequency band, while it is smaller (<0.2) in the middle and high frequency band. For ci of winding RD fault, it is larger (>0.2) in the low and middle frequency band, while it is smaller in the high frequency band. The changing trends of FRA signatures corresponding to three types of faults are totally diverse in each sub-frequency band; thus, there exist significant differences between the distributions of ci of binary images. The effect of various faults on correlation indicator corresponding to Fig. 13 is presented in Tab. 3, which shows obvious difference between three types of fault. This characteristic can be used to distinguish and recognize the types of winding inter-disk SC, DSV and RD faults by analyzing the distribution of ci in individual frequency range.

Advanced machine learning technique such as support vector machine (SVM) can be used to differentiate three fault types. SVM is suitable for processing the classification problem of small-scale samples. In this study, the performance of SVM has been initially tested. 42 groups of experimental data are divided into two categories, the training set and testing set. The training set is randomly selected, including 10 groups of inter-disk SC fault, 10 groups of DSV fault and 10 groups of RD fault. The rest of data consist of testing set, including 5 groups of inter-disk SC fault, 4 groups of DSV fault and 3 groups of RD fault. The basic element of training and testing set is the ci of binary images in three sub-frequency bands. Thus, the training set is a matrix of 30×3 and the testing set is a matrix of 12×3, a row of the matrix is expressed in (11), which is the input of SVM algorithm.

$$\begin{bmatrix} ci_{Low} & ci_{Mid} & ci_{High} \end{bmatrix} \quad (11)$$

The most frequently used radial basis function (RBF) has been chosen as the kernel function [28]. The parameter g of RBF and the penalty coefficient C are optimized by the grid searching and cross validation algorithm. Due to the test data is not massive, we construct 5 groups of different training and testing sets by randomly selecting from the data [24]. Thus, the optimal parameter g and C are different from each other in each specifically selected training and testing set. Fig. 14 shows the parameter optimization of g and C for a group of typical training and testing set, in which the optimal g and C are 0.125 and 4, respectively. The classification accuracies for 5 groups of testing sets are 100%, 91.7%,
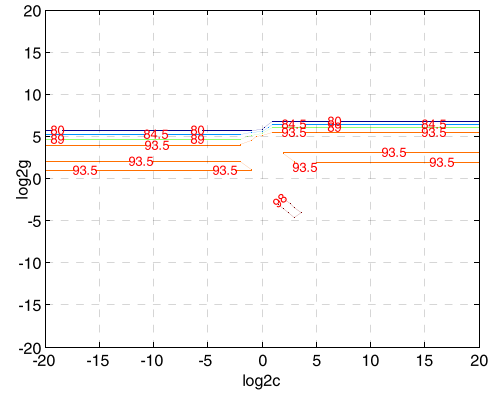

FIGURE 14. Parameter optimization of g and C for a group of typical training and testing set.

TABLE 4. Classification result of winding deformation fault types corresponding to one group of testing test (91.7%).

No.	Fault types	Diagnostic result
1	Inter-disk SC	Inter disk SC
2	Inter-disk SC	Inter disk SC
3	Inter-disk SC	Inter disk SC
4	Inter-disk SC	Inter disk SC
5	Inter-disk SC	Inter disk SC
6	RD	DSV
7	RD	RD
8	RD	RD
9	DSV	DSV
10	DSV	DSV
11	DSV	DSV
12	DSV	DSV
Accuracy rate		91.7%

91.7%, 100% and 100%. The classification result of winding deformation fault types corresponding to one group of testing set (91.7%) is shown in Tab. 4. The averaged classification accuracy of 5 groups is 96.7%, which initially demonstrates the SVM is capable of differentiating three fault types.

Moreover, a criterion for judging whether fault exists or not can be roughly derived from the above sample data. As the fault degree is smaller, the coincidence of two binary images in a certain sub-frequency band is higher, and the value of ci in this certain sub-frequency band is then larger. Thus, a threshold value of judging criterion can be derived from the boundaries of Fig. 13 in three axes, in which the ci around the boundaries corresponds to the winding minor deformation fault. If the ci of binary images in low frequency band $ci < 0.45$, the ci in middle frequency band $ci < 0.4$ or the ci in high frequency band $ci < 0.2$, it can be preliminary determined that there exists a certain fault in the tested winding.

V. APPLICATION OF PROPOSED METHOD ON LARGE OIL-IMMERSED POWER TRANSFORMER
A. ANALYSIS OF A 110 kV OIL-IMMERSED POWER TRANSFORMER
A 110 kV oil-immersed power transformer was out of service owing to the outlet short circuit fault. The amplitude–frequency and phase–frequency signatures of phase a and b
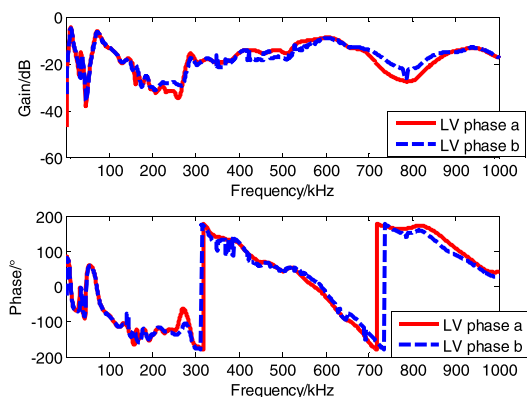
FIGURE 15. FRA amplitude-frequency and phase-frequency signature of a 110 kV oil-immersed power transformer.

TABLE 5. Relative factor, correlation indicator and diagnostic result corresponding to 110 KV power transformer frequency responses.

Method	Indicator	Frequency bands(kHz)			Diagnostic result
		1~100	100~600	600~1000	
FRA	R_{xy}	1.3964	1.3978	1.4854	Minor deformation
Binary image	ci	0.2275	0.1766	0.1920	Deformed

in 10 kV LV side were measured by an FRA analyzer, as shown in Fig. 15. The difference between two FRA signatures is significant, which indicates that there may be winding deformation fault in one phase winding. The relative factor R_{xy} of two FRA amplitude–frequency signatures in low, middle and high frequency band are calculated and listed in Tab. 5. According to the Chinese standard [12], the tested winding was diagnosed as a minor deformation.

Moreover, the FRA data are converted into binary images based on the proposed procedure, as shown in Fig. 16. It can be seen that the difference between two binary images of the middle frequency band is significant. The correlation indicators ci of two binary images in the low, middle and high frequency band are calculated and listed in Tab. 5. According to the criterion proposed in section IV, the tested winding was also diagnosed as deformed, which indicates that the diagnostic result obtained by the proposed method is similar to that obtained by the traditional FRA method when the difference of two FRA signatures is significant.

B. ANALYSIS OF A 220 kV OIL-IMMERSED POWER TRANSFORMER

A 220 kV oil-immersed power transformer was out of service. FRA amplitude–frequency and phase–frequency signatures of phase *a* winding were measured in 10 kV sides, as shown in Fig. 17 (marked in after fault). Fig. 17 also presents the reference FRA signature of the tested phase winding (marked in before fault). It is found that the difference between two FRA signatures is not significant. The relative factors R_{xy} of
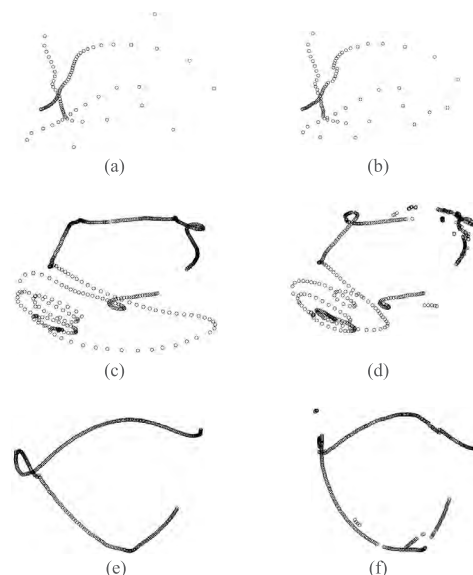

FIGURE 16. Frequency response binary image of LV phase *a* and *b* winding of a 110 kV oil-immersed power transformer. (a) 0 ~ 100 kHz of phase *a* winding, (b) 0 ~ 100 kHz of phase *b* winding, (c) 100 ~ 600 kHz of phase *a* winding, (d) 100 ~ 600 kHz of phase *b* winding, (e) 600 ~ 1000 kHz of phase *a* winding, (f) 600 ~ 1000 kHz of phase *b* winding.
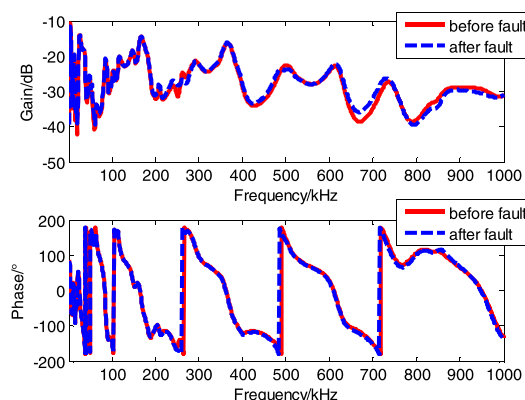

FIGURE 17. FRA amplitude–frequency and phase–frequency signature of a 220 kV oil-immersed power transformer.

two FRA amplitude–frequency signatures in the low, middle and high frequency band are calculated and presented in Tab. 6. However, according to the Chinese standard, this tested winding was diagnosed as healthy.

Moreover, the above FRA data are converted into binary images, as shown in Fig. 18. The correlation indicators of two binary images in the low, middle and high frequency band are calculated and presented in Tab. 6, respectively. According to the criterion proposed in section IV, the tested winding was diagnosed as deformed. The transformer was disassembled afterwards, and it was found that there exist some minor deformed parts on the exterior of tested phase *a* winding. The above analysis implies that the winding minor deformation fault sometimes cannot be detected by the traditional FRA method, while the proposed method shows a higher sensitivity to the winding minor fault.
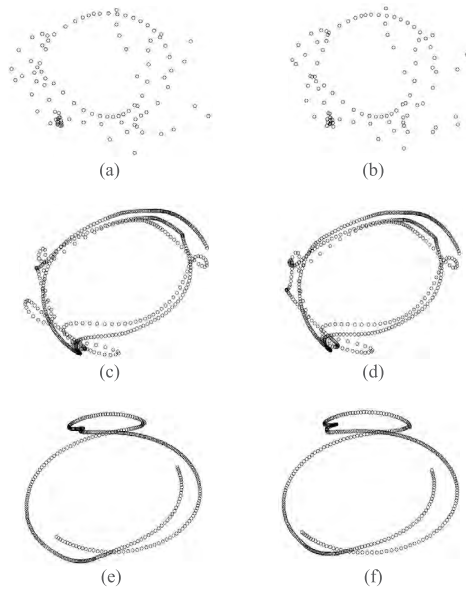
FIGURE 18. Frequency response binary image of LV phase *a* winding of a 220 kV oil-immersed power transformer obtained before and after a fault occurrence. (a) 0 ∼ 100 kHz image obtained before fault, (b) 0 ∼ 100 kHz image obtained after fault, (c) 100 ∼ 600 kHz image obtained before fault, (d) 100 ∼ 600 kHz image obtained after fault, (e) 600 ∼ 1000 kHz image obtained before fault, (f) 600 ∼ 1000 kHz image obtained after fault.

TABLE 6. relative factor, correlation indicator and diagnostic result corresponding to 220 KV power transformer frequency responses.

Method	Indicator	Frequency bands(kHz)			Diagnostic result
		1~100	100~600	600~1000	
FRA	R_{xy}	2.1525	1.9215	1.1524	Healthy
Binary image	*ci*	0.2587	0.3426	0.1321	Deformed

VI. DISCUSSION

This study successfully applied the digital image processing technique to analyze transformer winding deformation faults via several winding fault emulating experiments.

1) Although a criterion for judging whether faults exist or not has been proposed, given the limitations of current experimental conditions, the experimental sample data set is not massive. More experimental data and field cases are still needed to obtain a precise and accurate judging criterion. Nevertheless, the effectiveness of the method is demonstrated successfully. In addition, although the FRA data of two oil-immersed power transformers have been analyzed and evaluated, further research is still needed to include more data related to large power transformers to verify the reliability, repeatability and robustness of the binary image method.

2) There exist clear boundaries between the distributions of correlation indicator of binary images corresponding to three common fault types, and SVM has been successively demonstrated to differentiate these winding fault types. However, the winding deformation fault emulating experiments are confined to the inter-disk SC, DSV and RD fault, the actual winding deformation fault is not limited to these 3 categories. The distribution of correlation indicator corresponding to

other winding fault types such as axial deformation may be overlapped with the distribution area that corresponds to the above 3 categories. Nevertheless, the classifying and clustering characteristic of Fig. 13 can still be used to identify these main fault types.

3) The fault types and extent of winding deformation cannot be totally distinguished by the binary image method, but information of FRA amplitude–frequency and phase–frequency characteristic signatures are simultaneously utilized to improve the diagnostics of faults. Compared with the traditional FRA method, the binary image method is more sensitive to the winding fault.

4) In addition, Yousof *et al.* [29] discussed the possibility of FRA to detect transformer insulation aging, and found that the insulation aging will induce small variation of FRA curve in most frequency range, which is caused by the variation of winding capacitive component and dielectric permittivity. At present, frequency domain dielectric spectroscopy (FDS) measurement is the main technique to detect transformer insulation aging. The main frequency range of FDS is 1 mHz to 1 kHz, which is different from that of FRA (1 kHz to 1 MHz). Due to FRA is more sensitive to the transformer winding deformation in frequency range of 1 kHz to 1 MHz, the shift of FRA curve caused by insulation aging is significantly minor. Thus, it is possible to distinguish the winding deformation and insulation aging failure by simply analyzing the variation pattern of FRA curve. Nevertheless, the effect of insulation aging on the performance of the proposed method and the new threshold value can still be further studied in the next step.

VII. CONCLUSIONS

The FRA amplitude–frequency and phase–frequency information are combined and utilized in transformer winding deformation fault diagnostic method based on the frequency response binary image.

In the winding fault emulating experiments conducted on a specially designed and manufactured lego style transformer, the variations of FRA signatures of winding inter-disk SC, DSV and RD fault are shown to exhibit certain regularities. The distribution of correlation indicators of binary images in sub-frequency bands corresponding to 3 types of winding faults present classifying and clustering characteristics in a 3-dimensional space, which can be used to distinguish several common winding fault types. Advanced machine learning technique SVM has been successfully applied to classify these fault types.

The analyses of two actual large oil-immersed power transformer test cases demonstrate that the binary image method can be used to diagnose winding deformation faults in actual power transformers. Although the extents and locations of winding deformation fault cannot be totally determined at the present stage, this method can still be used to identify the fault types, similar to the traditional FRA method. Moreover, the higher sensitivity of the method can contribute to the accurate diagnosis of some minor winding deformation faults.

REFERENCES

[1] M. Bagheri, A. Zollanvari, and S. Nezhivenko, "Transformer fault condition prognosis using vibration signals over cloud environment," *IEEE Access.*, vol. 6, pp. 9862–9874, 2018.

[2] V. Behjat, A. Vahedi, A. Setayeshmehr, H. Borsi, and E. Gockenbach, "Diagnosing shorted turns on the windings of power transformers based upon online FRA using capacitive and inductive couplings," *IEEE Trans. Power Del.*, vol. 26, no. 4, pp. 2123–2133, Oct. 2011.

[3] B. García, J. C. Burgos, and Á. M. Alonso, "Winding deformations detection in power transformers by tank vibrations monitoring," *Electr. Power Syst. Res.*, vol. 74, no. 1, pp. 129–138, 2005.

[4] S. Mortazavian, M. M. Shabestary, Y. A.-R. I. Mohamed, and G. B. Gharehpetian, "Experimental studies on monitoring and metering of radial deformations on transformer HV winding using image processing and UWB transceivers," *IEEE Trans. Ind. Informat.*, vol. 11, no. 6, pp. 1334–1345, Dec. 2015.

[5] E. Arri, A. Carta, F. Mocci, and M. Tosi, "Diagnosis of the state of power transformer windings by on-line measurement of stray reactance," *IEEE Trans. Instrum. Meas.*, vol. 42, no. 2, pp. 372–378, Apr. 1993.

[6] A. Abu-Siada and S. Islam, "A novel online technique to detect power transformer winding faults," *IEEE Trans. Power Del.*, vol. 27, no. 2, pp. 849–857, Apr. 2012.

[7] V. A. Lavrinovich and A. V. Mytnikov, "Development of pulsed method for diagnostics of transformer windings based on short probe impulse," *IEEE Trans. Dielectr. Electr. Insul.*, vol. 22, no. 4, pp. 2041–2045, Aug. 2015.

[8] M. Bagheri, S. Nezhivenko, B. T. Phung, and T. Blackburn, "Air core transformer winding disk deformation: A precise study on mutual inductance variation and its influence on frequency response spectrum," *IEEE Access.*, vol. 6, pp. 7476–7488, 2018.

[9] E. Gomez-Luna, G. A. Mayor, C. Gonzalez-Garcia, and J. P. Guerra, "Current status and future trends in frequency-response analysis with a transformer in service," *IEEE Trans. Power Del.*, vol. 28, no. 2, pp. 1024–1031, Apr. 2013.

[10] M. Bagheri, M. S. Naderi, and T. Blackburn, "Advanced transformer winding deformation diagnosis: Moving from off-line to on-line," *IEEE Trans. Dielectr. Electr. Insul.*, vol. 19, no. 6, pp. 1860–1870, Dec. 2012.

[11] C. G. Yao et al., "Transformer winding deformation diagnostic system using online high frequency signal injection by capacitive coupling," *IEEE Trans. Dielectr. Electr. Insul.*, vol. 21, no. 4, pp. 1486–1492, Aug. 2014.

[12] *Frequency Response Analysis on Winding Deformation of Power Transformers*, document DL/T911-2004, ICS27.100, F24, 2005-15182, (in Chinese), People Republic of China, Electric Power Industry Standard, 2005.

[13] *Measurement of Frequency Response*, IEC Standard 60076-18, Ed. 1.0, 2012.

[14] W. H. Portilla, G. A. Mayor, J. P. Guerra, and C. Gonzalez-Garcia, "Detection of transformer faults using frequency-response traces in the low-frequency bandwidth," *IEEE Trans. Ind. Electron.*, vol. 61, no. 9, pp. 4971–4978, Sep. 2014.

[15] M. Wang, A. J. Vandermaar, and K. D. Srivastava, "Improved detection of power transformer winding movement by extending the FRA high frequency range," *IEEE Trans. Power Del.*, vol. 20, no. 3, pp. 1930–1938, Jul. 2005.

[16] R. K. Senobari, J. Sadeh, and H. Borsi, "Frequency response analysis (FRA) of transformers as a tool for fault detection and location: A review," *Electr. Power Syst. Res.*, vol. 155, pp. 172–183, Feb. 2018.

[17] M. H. Samimi, S. Tenbohlen, A. A. S. Akmal, and H. Mohseni, "Improving the numerical indices proposed for the FRA interpretation by including the phase response," *Int. J. Electr. Power Energy Syst.*, vol. 83, pp. 585–593, Dec. 2016.

[18] O. Aljohani and A. Abu-Siada, "Application of digital image processing to detect short-circuit turns in power transformers using frequency response analysis," *IEEE Trans. Ind. Informat.*, vol. 12, no. 6, pp. 2062–2073, Dec. 2016.

[19] A. Abu-Siada and O. Aljohani, "Detecting incipient radial deformations of power transformer windings using polar plot and digital image processing," *IET Sci., Meas. Technol.*, vol. 12, no. 4, pp. 492–499, 2018.

[20] O. Aljohani and A. Abu-Siada, "Application of digital image processing to detect transformer bushing faults and oil degradation using FRA polar plot signature," *IEEE Trans. Dielectr. Electr. Insul.*, vol. 24, no. 1, pp. 428–436, Feb. 2017.

[21] Z. Zhao, C. Yao, C. Li, and S. Islam, "Detection of power transformer winding deformation using improved FRA based on binary morphology and extreme point variation," *IEEE Trans. Ind. Electron.*, vol. 65, no. 4, pp. 3509–3519, Apr. 2018.

[22] V. Behjat and M. Mahvi, "Statistical approach for interpretation of power transformers frequency response analysis results," *IET Sci., Meas. Technol.*, vol. 9, no. 3, pp. 367–375, 2015.

[23] M. Bagheri, M. S. Naderi, T. Blackburn, and T. Phung, "Frequency response analysis and short-circuit impedance measurement in detection of winding deformation within power transformers," *IEEE Elect. Insul. Mag.*, vol. 29, no. 3, pp. 33–40, May 2013.

[24] Z. Zhao, C. Tang, Q. Zhou, L. Xu, Y. Gui, and C. Yao, "Identification of power transformer winding mechanical fault types based on online IFRA by support vector machine," *Energies*, vol. 10, no. 12, p. 2022, 2017.

[25] A. Abu-Siada, N. Hashemnia, S. Islam, and M. A. S. Masoum, "Understanding power transformer frequency response analysis signatures," *IEEE Elect. Insul. Mag.*, vol. 29, no. 3, pp. 48–56, May 2013.

[26] N. Hashemnia, A. Abu-Siada, and S. Islam, "Improved power transformer winding fault detection using FRA diagnostics—Part 2: Radial deformation simulation," *IEEE Trans. Dielectr. Electr. Insul.*, vol. 22, no. 1, pp. 564–570, Feb. 2015.

[27] E. Rahimpour, J. Christian, K. Feser, and H. Mohseni, "Transfer function method to diagnose axial displacement and radial deformation of transformer windings," *IEEE Trans. Power Del.*, vol. 18, no. 2, pp. 493–505, Apr. 2003.

[28] M. Bigdeli, M. Vakilian, and E. Rahimpour, "Transformer winding faults classification based on transfer function analysis by support vector machine," *IET Electr. Power Appl.*, vol. 6, no. 5, pp. 268–276, May 2012.

[29] M. F. M. Yousof, C. Ekanayake, and T. K. Saha, "Examining the ageing of transformer insulation using FRA and FDS techniques," *IEEE Trans. Dielectr. Electr. Insul.*, vol. 22, no. 2, pp. 1258–1265, Apr. 2015.

ZHONGYONG ZHAO was born in Guangyuan, Sichuan, China. He received the B.Sc. and Ph.D. degrees from Chongqing University, Chongqing, China, in 2011 and 2017, respectively, all in electrical engineering. He received the scholarship from China Scholarship Council to enable him to attend a joint-training Ph.D. program at Curtin University, Perth, Australia, from 2015 to 2016. He is currently an Associate Professor with the College of Engineering and Technology, Southwest University, Chongqing, China. His current research interests include condition monitoring and fault diagnosing for HV apparatus, and pulsed power technology.

CHENGUO YAO (M'08) was born in Nanchong, Sichuan, China. He received the B.S., M.S., and Ph.D. degrees in electrical engineering from Chongqing University, Chongqing, China, in 1997, 2000, and 2003, respectively. He became a Professor with the School of Electrical Engineering, Chongqing University, in 2007. He was a Visiting Scholar with Old Dominion University, USA, from 2017 to 2018. His current research interests include online monitoring of insulation condition and insulation fault diagnosis for HV apparatus, pulsed power technology, and its application in biomedical engineering.

CHAO TANG was born in Sichuan, China, in 1981. He received the M.S. and Ph.D. degrees in electrical engineering from Chongqing University, China, in 2007 and 2010, respectively. As a Ph.D. student, from 2008 to 2009, and as a Visiting Scholar, from 2013 to 2013 and from 2015 to 2016, he studied in the Tony Davies High Voltage Lab, University of Southampton, U.K., doing some researches on the dielectric response characteristics and space charge behaviors of oil-paper insulation. He is currently a Professor with the College of Engineering Technology, Southwest University, China. His research interest includes online monitoring of insulation conditions and fault diagnosis for high-voltage equipment.

CHENGXIANG LI was born in Shandong, China. He received the B.S., M.S., and Ph.D. degrees in electrical engineering from Chongqing University, Chongqing, China, in 2002, 2005, and 2011, respectively. He is currently an Associate Professor with the School of Electrical Engineering, Chongqing University. His current research interests include pulse power technology and its application in biomedical engineering, and online monitoring of insulation condition for HV apparatus.

FAYOU YAN received the B.Sc. degree from Tianjin University and the Ph.D. degree in electrical engineering from the China Electric Power Research Institute, Beijing, China, in 2011 and 2016, respectively. He is currently a Lecturer with the Department of Electrical Engineering, College of Engineering and Technology, Southwest University. His current research interests include modular multilevel converter, and control and protection of HVDC grid.

SYED ISLAM received the B.Sc. degree in electrical engineering from the Bangladesh University of Engineering and Technology, Bangladesh, in 1979, and the M.Sc. and Ph.D. degrees in electrical power engineering from the King Fahd University of Petroleum and Minerals, Dhahran, Saudi Arabia, in 1983 and 1988, respectively.

He has been a Visiting Professor with the Shanghai University of Electrical Power, China. He is currently the Dean of the School of Science Engineering and Information Technology, Federation University Australia, Australia. He received the Dean's medallion for research at Curtin University, in 1999. He has published more than 300 technical papers in his area of expertise. His research interests include condition monitoring of transformers, wind energy conversion, and smart power systems.

Dr. Islam is also a member of the Steering Committee of the Australian Power Institute and a member of the WA EESA board. He is a Fellow of the Engineers Australia, a Fellow of the IET, and a Chartered Engineer in U.K. He received the IEEE T Burke Haye's Faculty Recognition Award, in 2000. He received the Curtin University Inaugural Award for Research Development, in 2012. He received the Sir John Madsen Medal, in 2011 and 2014 for the Best Electrical Engineering Paper in Australia. He is a Founding Editor of the IEEE TRANSACTION ON SUSTAINABLE ENERGY and an Associate Editor of the *IET Renewable Power Generation*. He was the Guest Editor in Chief for the IEEE TRANSACTION ON SUSTAINABLE ENERGY special issue on Variable Power Generation Integration into Grid. He has been a keynote speaker and invited speaker at many international workshops and conferences.

●●●